SCIENCE CHINA
Information Sciences

• RESEARCH PAPER •

February 2024, Vol. 67, Iss. 2, 122303:1–122303:13
https://doi.org/10.1007/s11432-023-3833-x

Analysis of phase preservation and interferometric offset test in sparse SAR imaging

Zhongqiu XU[1,2,3], Bingchen ZHANG[1,2,3], Guangzuo LI[1,2*], Xueli ZHAN[2], Yanfei BAO[4] & Yirong WU[1,2,3]

[1]*Key Laboratory of Spatial Information Processing and Application System Technology, Chinese Academy of Sciences, Beijing* 100190*, China;*
[2]*Aerospace Information Research Institute, Chinese Academy of Sciences, Beijing* 100190*, China;*
[3]*School of Electronic, Electrical and Communication Engineering, University of Chinese Academy of Sciences, Beijing* 100190*, China;*
[4]*PLA Academy of Military Sciences, Beijing* 100191*, China*

Received 10 February 2023/Revised 7 June 2023/Accepted 23 July 2023/Published online 25 January 2024

Abstract Sparse synthetic aperture radar (SAR) imaging has emerged as a reliable microwave imaging scheme in the recent decade and excels in down-sampling reconstruction and full-sampling performance improvements such as noise, sidelobe, speckle, and ambiguity suppression. To utilize complex image products of sparse reconstruction for improvement in polarimetric, interferometric, and tomographic SAR imaging, it is necessary to evaluate the phase preservation of sparse SAR imaging. In this study, we first introduce the general alternating direction method of multipliers (ADMM) as the universal framework for sparse reconstruction algorithms and adopt chirp scaling algorithm (CSA)-based azimuth-range decouple operators to avoid expensive data storage and processing. Further, we theoretically analyze the phase preservation of the sparse reconstruction algorithm through a comparison with the reconstruction results of CSA. Finally, we conduct the interferometric offset test on the sparse reconstruction results of simulated and real Gaofen-3 (GF-3) SAR data, demonstrating the phase-preserving ability of sparse methods.

Keywords sparse SAR imaging, phase preservation, interferometric offset test, general ADMM, azimuth-range decouple

1 Introduction

Synthetic aperture radar (SAR) imaging is an active airborne and spaceborne remote sensing technology and has a broad range of applications, from environmental protection and disaster monitoring to ocean observations and geological mapping. As the demand for high observation resolution and swath width increases, the development of SAR systems encounters bottlenecks owing to the radar resolving theory and Nyquist-Shannon sampling theorem [1]. Consequently, sparse SAR imaging gradually emerged as a popular research topic [2–4].

Sparse SAR imaging is an emerging microwave imaging scheme in the recent decade that integrates the sparse signal processing method and SAR imaging for down-sampling reconstruction and full-sampling performance improvement. Furthermore, it has been successfully applied to multiple SAR imaging modes [5,6]. Oriented toward various applications, sparse SAR imaging can utilize appropriate sparsity in the spatial or transform domain as prior information in the optimization problem, which is typically implemented via regularization. Typical applications include feature enhancement of point and distributed targets and suppression of azimuth ambiguity, corresponding to spatial, gradient, and group sparsity, respectively. As the representative of the above three sparsity constraints, ℓ_1, total variation (TV), and $\ell_{2,1}$ regularization are widely used in sparse reconstruction [7–9].

In various spatial sparse constraints, ℓ_0 norm is the most suitable choice because it can directly return the number of nonzero coefficients. Unfortunately, ℓ_0 regularization is a nondeterministic polynomial-time hard (NP-hard) problem, and hence, the penalty function must be relaxed to render the problem

* Corresponding author (email: ligz@aircas.ac.cn)

mathematically solvable. Consequently, the relaxed ℓ_1 regularization becomes an efficient tool for spatial sparse reconstruction because of its solvability and equivalence with ℓ_0 regularization under certain conditions [10]. When adopted in SAR imaging, ℓ_1 regularization can suppress additive noise and sidelobes, thereby enhancing the point targets-based features such as the target background ratio (TBR) [11]. However, the single ℓ_1 norm constraint applies only to feature enhancement of point targets in spatial sparse scenes, while ignoring features of distributed targets. Therefore, the TV norm of the image magnitude is introduced as the gradient sparse constraint in the SAR imaging model. Benefiting from the suppression of speckles by TV regularization, ℓ_1-TV realizes feature enhancement of distributed targets as well as point targets, such as the equivalent number of looks (ENL) [12]. Furthermore, the azimuth ambiguity has always puzzled researchers in SAR imaging and applications. To solve this issue, in $\ell_{2,1}$ regularization, the group sparsity between the target area and ± 1 ambiguity area is utilized to suppress ambiguity, thereby considerably reducing azimuth ambiguity signal ratio (AASR) [13].

Sparse SAR imaging has been proven effective through the assessment of parameters such as TBR, ENL, and AASR. However, these traditional quality requirements for sparse SAR imaging are primarily based on amplitude measurements and ignore the phase. Over the years, SAR polarization, interferometry, and tomography have become increasingly popular, which all need to utilize the phase information in SAR complex products [14]. Compared with the matched filtering method, two-dimensional sparse reconstruction is more advantageous for noise, sidelobe, speckle, and ambiguity suppression. Thus, there is potential to improve the performance of polarimetric, interferometric, and tomographic SAR imaging based on the results of sparse reconstruction [15–17]. Accordingly, there is a need to evaluate the phase preservation of sparse SAR imaging, so that we can utilize its results for more in-depth work. In the research [18], the interferometric offset test was proposed to evaluate the phase preservation of four different ERS SAR processors. Based on this, the authors in [19] extended the test to different acquisition modes, namely StripMAP, ScanSAR, TopSAR, and SPOTLIGHT. However, no research or testing on the phase preservation of sparse reconstruction has been conducted.

The considerations and major contributions of our study are as follows:

First, we introduced the general alternating direction method of multipliers (ADMM) as the universal framework for sparse reconstruction algorithms [20, 21]. Compared with other algorithms, such as iterative shrinkage and thresholding algorithm (ISTA) and complex approximate message passing (CAMP) algorithm [5], ADMM has better compatibility with various regularization problems, including ℓ_1, ℓ_1-TV, and $\ell_{2,1}$. In addition, the unified framework can facilitate the analysis of phase preservation.

Second, to simplify the phase preservation analysis, we adopted the chirp scaling algorithm (CSA)-based azimuth-range decouple operators to substitute the measurement matrix and its Hermitian transpose, which can establish an association between sparse reconstruction and CSA [22,23]. Furthermore, in large-scale SAR imaging applications, the volume of the observation matrix generally exceeds $10^6 \times 10^6$. The decouple scheme can avoid huge resource consumption in storage and calculation to accelerate signal processing.

Third, since it has been proven that CSA preserves phase, we theoretically analyzed the phase preservation of the sparse reconstruction algorithm represented by the general ADMM framework based on azimuth-range decouple in a stepwise manner by comparing with reconstruction results of CSA.

Finally, we processed the simulated and real Gaofen-3 (GF-3) SAR data using sparse methods, conducted the interferometric offset test on imaging results, and demonstrated the phase-preserving capability of the sparse reconstruction algorithm.

The remainder of this paper is structured as follows: In Section 2, we introduce the sparse reconstruction model for SAR imaging and focus on the three commonly used sparse constraints. In Section 3, we first present the general ADMM framework-based sparse reconstruction algorithm, then derive its combination with azimuth-range decouple operators in detail, and finally theoretically analyze the phase preservation of the developed algorithm. In Section 4, we present the results of experiments and performance analysis conducted to verify the phase preservation characteristics of sparse reconstruction. Finally, the conclusion and future work are discussed in Section 5.

2 Reconstruction models of sparse SAR imaging

The SAR observation model suitable for sparse signal processing framework can be expressed as [1]

$$\boldsymbol{y} = \boldsymbol{H}\boldsymbol{x} + \boldsymbol{n}, \tag{1}$$

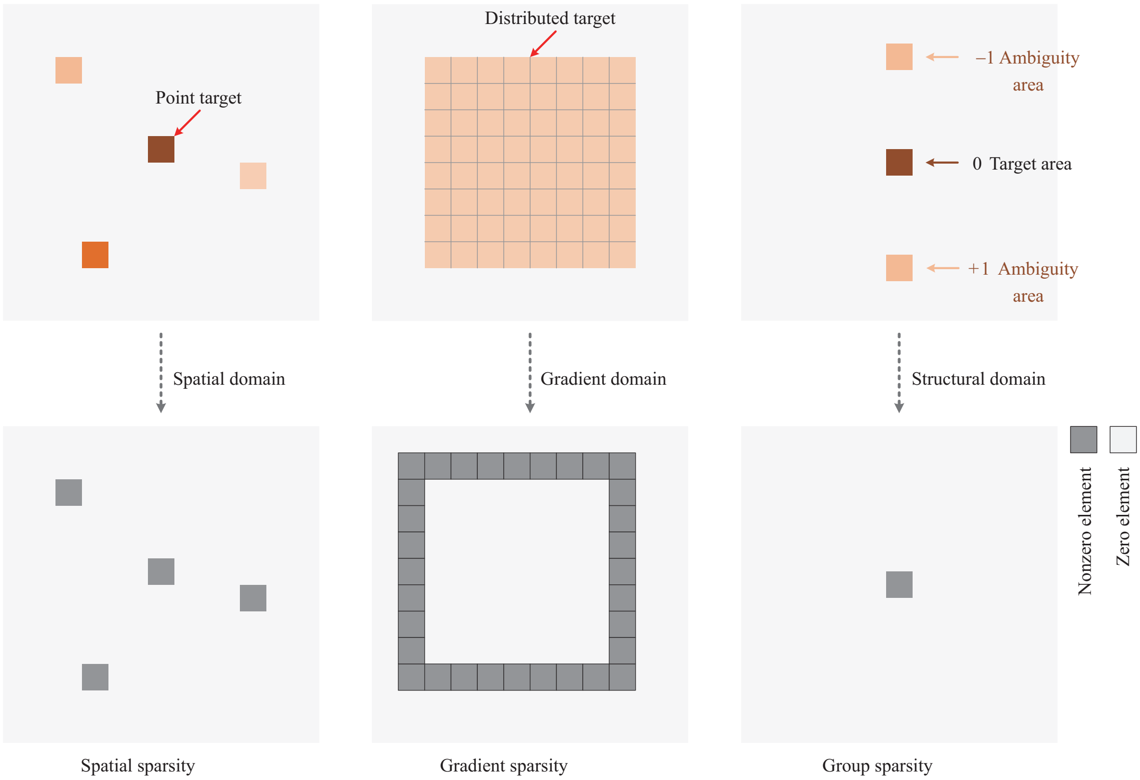

Figure 1 (Color online) Diagram of sparsity in spatial, gradient, and structural domains.

where $\boldsymbol{x} = \mathrm{vec}(\boldsymbol{X}) \in \mathbb{C}^{N_a N_r \times 1}$ and $\boldsymbol{X} \in \mathbb{C}^{N_a \times N_r}$ denote the complex-valued reflectivity of the surveillance region, $\boldsymbol{y} = \mathrm{vec}(\boldsymbol{Y}) \in \mathbb{C}^{N_\eta N_\tau \times 1}$ and $\boldsymbol{Y} \in \mathbb{C}^{N_\eta \times N_\tau}$ denote the sampled echo data, $\mathrm{vec}(\cdot)$ represents the vectorization along the range direction, and $\boldsymbol{n}$ is the additive noise vector. And $\boldsymbol{H}$ is the corresponding measurement matrix of the SAR system, determined by the waveform of the transmitted signal, the geometric relationship between the radar and the observation scene, as well as the sampling scheme. In this paper, considering that linear frequency modulation (LFM) signal is the commonly used waveform for SAR system, the measurement matrix $\boldsymbol{H}$ is therefore constructed as the chirp signal-based matrix, whose structure can be adjusted according to different SAR imaging modes and down-sampling schemes.

The reconstruction model of joint feature-enhanced sparse SAR imaging can be written as the following compound regularization form:

$$\min_{\boldsymbol{x}} \|\boldsymbol{y} - \boldsymbol{H}\boldsymbol{x}\|_2^2 + \sum_{i}^{N} \lambda_i p_i(\boldsymbol{x}), \tag{2}$$

where $p_i(\boldsymbol{x})$ is the penalty function which is selected according to the demand of feature enhancement, and λ_i is the regularization parameter. As shown in Figure 1, spatial sparsity, gradient sparsity, and group sparsity are the three most commonly used sparse priors in the reconstruction model.

Firstly, for feature enhancement of point targets, ℓ_1 norm is the typical penalty reflecting spatial sparsity [1, 11],

$$\min_{\boldsymbol{x}} \|\boldsymbol{y} - \boldsymbol{H}\boldsymbol{x}\|_2^2 + \lambda \|\boldsymbol{x}\|_1, \tag{3}$$

$$\|\boldsymbol{x}\|_1 = \sum_{m}^{N_a N_r} |x_m|. \tag{4}$$

Then, for feature enhancement of distributed targets, TV norm is the typical gradient sparse constraint [8, 21],

$$\min_{\boldsymbol{x}} \|\boldsymbol{y} - \boldsymbol{H}\boldsymbol{x}\|_2^2 + \lambda_1 \|\boldsymbol{x}\|_1 + \lambda_2 \mathrm{TV}(|\boldsymbol{x}|), \tag{5}$$

$$\mathrm{TV}(|\boldsymbol{x}|) = \sum_{a,r}^{N_a, N_r} \sqrt{(|X_{a+1,r}| - |X_{a,r}|)^2 + (|X_{a,r+1}| - |X_{a,r}|)^2}, \tag{6}$$

where $X_{a,r}$ represents the element in the ath-row and rth-column.

And for suppression of azimuth ambiguity, $\ell_{2,1}$ is the typical group sparse constraint [9, 13],

$$\min_{\boldsymbol{x}} \|\boldsymbol{y}-\boldsymbol{H}\boldsymbol{x}\|_2^2+\lambda\|\boldsymbol{x}\|_{2,1}, \tag{7}$$

$$\|\boldsymbol{x}\|_{2,1}=\sum_{m}^{N_aN_r}\left(|(x_{-1})_m|^2+|(x_0)_m|^2+|(x_{+1})_m|^2\right)^{\frac{1}{2}}, \tag{8}$$

where $\boldsymbol{H}=[\boldsymbol{H}_{-1},\boldsymbol{H}_0,\boldsymbol{H}_{+1}]$ comprises measurement matrices of target area and ±1 ambiguity area, and then $\boldsymbol{x}=[\boldsymbol{x}_{-1}^{\mathrm{T}},\boldsymbol{x}_0^{\mathrm{T}},\boldsymbol{x}_{+1}^{\mathrm{T}}]^{\mathrm{T}}$.

3 Analysis of phase preservation based on sparse reconstruction algorithms

3.1 General ADMM framework based sparse reconstruction

In this subsection, we introduce the general ADMM framework to solve the optimization problem (2) and theoretically analyze the phase preservation based on the framework [20, 21]. According to the variable splitting scheme [24], Eq. (2) can be converted to the following equivalent problem:

$$\min_{\boldsymbol{x}} \|\boldsymbol{y}-\boldsymbol{H}\boldsymbol{x}\|_2^2+\sum_{i}^{N}\lambda_i p_i(\boldsymbol{z}_i) \quad \text{s.t. } G\boldsymbol{x}=\boldsymbol{z}, \tag{9}$$

where $G=[I^{\mathrm{T}},\ldots,I^{\mathrm{T}}]^{\mathrm{T}}$, $\boldsymbol{z}=[\boldsymbol{z}_1^{\mathrm{T}},\ldots,\boldsymbol{z}_N^{\mathrm{T}}]^{\mathrm{T}}$, and I is the identity matrix. As shown above, variable splitting is a very simple procedure that consists of creating a new variable, say the auxiliary variable $\boldsymbol{z}$, to serve as the argument of penalty functions $\{p_i|i=1,2,\ldots,N\}$ under the constraint that $G\boldsymbol{x}=\boldsymbol{z}$. Then the augmented Lagrangian multiplier (ALM) method-based objective function can be written as

$$\begin{aligned}\mathcal{L}(\boldsymbol{x},\boldsymbol{z},\boldsymbol{\lambda},\mu)&=\|\boldsymbol{y}-\boldsymbol{H}\boldsymbol{x}\|_2^2+\sum_{i}^{N}\lambda_i p_i(\boldsymbol{z}_i)+\boldsymbol{\lambda}^{\mathrm{T}}(\boldsymbol{z}-G\boldsymbol{x})+\frac{\mu}{2}\|G\boldsymbol{x}-\boldsymbol{z}\|_2^2\\&=\|\boldsymbol{y}-\boldsymbol{H}\boldsymbol{x}\|_2^2+\sum_{i}^{N}\lambda_i p_i(\boldsymbol{z}_i)+\mu\cdot\frac{\boldsymbol{\lambda}^{\mathrm{T}}}{\mu}(\boldsymbol{z}-G\boldsymbol{x})+\frac{\mu}{2}\|G\boldsymbol{x}-\boldsymbol{z}\|_2^2,\end{aligned} \tag{10}$$

where $\boldsymbol{\lambda}$ is the Lagrange multiplier vector and μ is the augmented Lagrangian penalty parameter. For convenience, let $\boldsymbol{d}=\frac{\boldsymbol{\lambda}}{\mu}$, $f(\boldsymbol{x})=\|\boldsymbol{y}-\boldsymbol{H}\boldsymbol{x}\|_2^2$, and then Eq. (10) can be rewritten as

$$\begin{aligned}\mathcal{L}(\boldsymbol{x},\boldsymbol{z},\boldsymbol{d},\mu)&=f(\boldsymbol{x})+\sum_{i}^{N}\lambda_i p_i(\boldsymbol{z}_i)+\mu\boldsymbol{d}^{\mathrm{T}}(\boldsymbol{z}-G\boldsymbol{x})+\frac{\mu}{2}\|G\boldsymbol{x}-\boldsymbol{z}\|_2^2\\&=f(\boldsymbol{x})+\sum_{i}^{N}\lambda_i p_i(\boldsymbol{z}_i)+\frac{\mu}{2}\left[\|G\boldsymbol{x}-\boldsymbol{z}\|_2^2-2\boldsymbol{d}^{\mathrm{T}}(G\boldsymbol{x}-\boldsymbol{z})+\|\boldsymbol{d}\|_2^2\right]-\frac{\mu}{2}\|\boldsymbol{d}\|_2^2\\&=f(\boldsymbol{x})+\sum_{i}^{N}\lambda_i p_i(\boldsymbol{z}_i)+\frac{\mu}{2}\|G\boldsymbol{x}-\boldsymbol{z}-\boldsymbol{d}\|_2^2-\frac{\mu}{2}\|\boldsymbol{d}\|_2^2.\end{aligned} \tag{11}$$

Naturally, the optimization of the objective function (11) can be divided into the three subproblems in (12), and then be solved alternately:

$$\begin{aligned}&\text{(a) } \boldsymbol{x}^{(t+1)}=\arg\min_{\boldsymbol{x}}\ \mathcal{L}(\boldsymbol{x},\boldsymbol{z}^{(t)},\boldsymbol{d}^{(t)},\mu),\\&\text{(b) } \boldsymbol{z}_i^{(t+1)}=\arg\min_{\boldsymbol{z}_i}\ \mathcal{L}(\boldsymbol{x}^{(t+1)},\boldsymbol{z},\boldsymbol{d}^{(t)},\mu),\\&\text{(c) } \boldsymbol{d}^{(t+1)}=\arg\max_{\boldsymbol{d}}\ g(\boldsymbol{d}),\end{aligned} \tag{12}$$

where $g(\boldsymbol{d})=\mathcal{L}(\boldsymbol{x}^{(t+1)},\boldsymbol{z}^{(t+1)},\boldsymbol{d},\mu)$ is the Lagrangian dual function. Next, we present solutions to the three subproblems in turn.

Table 1 Proximal operators for different penalties

Penalty	Proximal operator: $\Psi(x,\lambda)$
ℓ_1 norm	$\mathrm{sign}(x)\cdot\max(\lvert x\rvert-\lambda,0)$
ℓ_1-TV norm [8]	$\mathrm{sign}(x)\cdot(\lvert x\rvert-\lambda\cdot f_{\mathrm{TV}}(\lvert x\rvert))$
$\ell_{2,1}$ norm	$\mathrm{sign}(x)\cdot(\lvert x\rvert-\frac{\lambda\cdot\lvert x\rvert}{\max\{x_{\mathrm{hybrid}},\lambda\}})$

Subproblem (a) in (12) can be simplified as a quadratic programming problem. In this paper, we use the gradient descent (GD) algorithm to solve the problem instead of the least squares, so as to prepare for the combination of decouple operators in Subsection 3.2 [25]:

$$\begin{aligned}
\boldsymbol{x}^{(t+1)} &= \arg\min_{\boldsymbol{x}}\ \mathcal{L}(\boldsymbol{x},\boldsymbol{z}^{(t)},\boldsymbol{d}^{(t)},\mu)\\
&= \arg\min_{\boldsymbol{x}} f(\boldsymbol{x})+\frac{\mu}{2}\left\|G\boldsymbol{x}-\boldsymbol{z}^{(t)}-\boldsymbol{d}^{(t)}\right\|_2^2\\
&= \arg\min_{\boldsymbol{x}}\ \left\|\begin{bmatrix}\sqrt{\frac{\mu}{2}}\boldsymbol{G}\\ \boldsymbol{H}\end{bmatrix}\boldsymbol{x}-\begin{bmatrix}\sqrt{\frac{\mu}{2}}(\boldsymbol{z}^{(t)}+\boldsymbol{d}^{(t)})\\ \boldsymbol{y}\end{bmatrix}\right\|_2^2=\arg\min_{\boldsymbol{x}}\ \left\|\overline{\boldsymbol{H}}\boldsymbol{x}-\boldsymbol{\beta}\right\|_2^2\\
&= \boldsymbol{x}^{(t)}-\frac{1}{L}\nabla_{\boldsymbol{x}}\left[\left\|\overline{\boldsymbol{H}}\boldsymbol{x}-\boldsymbol{\beta}\right\|_2^2\right]=\boldsymbol{x}^{(t)}+\frac{1}{L}\overline{\boldsymbol{H}}^{\mathrm{H}}(\boldsymbol{\beta}-\overline{\boldsymbol{H}}\boldsymbol{x}^{(t)})\\
&= \boldsymbol{x}^{(t)}+\frac{1}{L}\left[\frac{\mu}{2}\sum_{i}^{N}(\boldsymbol{z}_i^{(t)}+\boldsymbol{d}_i^{(t)})-\frac{\mu}{2}N\boldsymbol{x}^{(t)}+\boldsymbol{H}^{\mathrm{H}}(\boldsymbol{y}-\boldsymbol{H}\boldsymbol{x}^{(t)})\right],
\end{aligned}\tag{13}$$

where $\frac{1}{L}$ represents the step size.

Subproblem (b) in (12) is the Moreau proximal mapping prox_{p_i} for the penalty function $p_i(\cdot)$, whose closed-form solution Ψ_{p_i} has been given in Table 1 [21],

$$\begin{aligned}
\boldsymbol{z}_i^{(t+1)} &= \arg\min_{\boldsymbol{z}_i}\ \mathcal{L}(\boldsymbol{x}^{(t+1)},\boldsymbol{z},\boldsymbol{d}^{(t)},\mu)\\
&= \arg\min_{\boldsymbol{z}_i}\lambda_i p_i(\boldsymbol{z}_i)+\frac{\mu}{2}\left\|I\cdot\boldsymbol{x}^{(t+1)}-\boldsymbol{z}_i-\boldsymbol{d}_i^{(t)}\right\|_2^2=\arg\min_{\boldsymbol{z}_i}\lambda_i p_i(\boldsymbol{z}_i)+\frac{\mu}{2}\left\|\left(\boldsymbol{x}^{(t+1)}-\boldsymbol{d}_i^{(t)}\right)-\boldsymbol{z}_i\right\|_2^2\\
&= \mathrm{prox}_{p_i}\left(\boldsymbol{x}^{(t+1)}-\boldsymbol{d}_i^{(t)}\right)=\Psi_{p_i}\left(\boldsymbol{x}^{(t+1)}-\boldsymbol{d}_i^{(t)},\frac{\lambda_i}{\mu}\right).
\end{aligned}\tag{14}$$

As shown in Table 1, the proximal operators for the three typical penalties all consist of two parts: the left part $\mathrm{sign}(x)$ represents the phase of the input complex data x, and the right part only performs operations on $|x|$, which is the amplitude of x. For ℓ_1 norm and $\ell_{2,1}$ norm, the amplitude-operation is essentially a thresholding process on non-negative real data, in which the thresholding function can maintain the positive or negative attributes of the data. For ℓ_1-TV norm, according to the lemma in [21], as the input $|x|$ is non-negative, the output of its amplitude-operation will definitely be non-negative. Therefore, the three proximal operators are all phase-preserving operations that only affect the amplitude without changing the phase.

Besides, the typical penalties in the popular nonconvex regularization, such as the minimax concave (MC) penalty and the smoothly clipped absolute deviation (SCAD) penalty, have the same form and property of proximal operators as ℓ_1 norm. As a consequence, the conclusion of phase preservation can also be extended to the proximal operators for penalty functions in nonconvex regularization satisfying the above conditions.

Subproblem (c) in (12) aims to solve $\boldsymbol{d}$ (the variant of the Lagrange multiplier vector $\boldsymbol{\lambda}$) by maximizing the Lagrangian dual function [20]. The dual problem can be solved by the gradient ascent method, as shown in the last line of (15):

$$\begin{aligned}\boldsymbol{d}^{(t+1)} &= \arg\max_{\boldsymbol{d}} \ \mathcal{L}(\boldsymbol{x}^{(t+1)}, \boldsymbol{z}^{(t+1)}, \boldsymbol{d}, \mu) \\ &= \arg\max_{\boldsymbol{d}} \ \left[\mu \boldsymbol{d}^{\mathrm{T}}\left(\boldsymbol{z}^{(t+1)} - G\boldsymbol{x}^{(t+1)}\right)\right] = \arg\max_{\boldsymbol{d}} \ \left[\boldsymbol{d}^{\mathrm{T}}\left(\boldsymbol{z}^{(t+1)} - G\boldsymbol{x}^{(t+1)}\right)\right] \\ &= \boldsymbol{d}^{(t)} + \frac{1}{L'}\nabla_{\boldsymbol{d}}\left[\boldsymbol{d}^{\mathrm{T}}\left(\boldsymbol{z}^{(t+1)} - G\boldsymbol{x}^{(t+1)}\right)\right] = \boldsymbol{d}^{(t)} + \frac{1}{L'}\left(\boldsymbol{z}^{(t+1)} - G\boldsymbol{x}^{(t+1)}\right),\end{aligned} \tag{15}$$

where $\frac{1}{L'}$ represents the step size.

Above all, the general ADMM framework-based sparse reconstruction is summarized in Algorithm 1.

Algorithm 1 General ADMM framework-based sparse reconstruction

Input: The echo data $\boldsymbol{y}$, the initial solution $\boldsymbol{x}^{(0)} = \boldsymbol{0}$, $\boldsymbol{z}_i^{(0)} = \boldsymbol{0}$, $\boldsymbol{d}_i^{(0)} = \boldsymbol{0}$, the measurement matrix $\boldsymbol{H}$ and its Hermitian transpose $\boldsymbol{H}^{\mathrm{H}}$, the error parameter ϵ, and the minimum and maximum number of iteration $t \in [0, T_{\max}]$.

1: **while** res $\geqslant \epsilon$ and $t \leqslant T_{\max}$ **do**
2: $\quad \boldsymbol{x}^{(t+1)} = \boldsymbol{x}^{(t)} + \frac{1}{L}[\frac{\mu}{2}\sum_i^N(\boldsymbol{z}_i^{(t)} + \boldsymbol{d}_i^{(t)}) - \frac{\mu}{2}N\boldsymbol{x}^{(t)} + \boldsymbol{H}^{\mathrm{H}}(\boldsymbol{y} - \boldsymbol{H}\boldsymbol{x}^{(t)})]$;
3: $\quad \boldsymbol{z}_i^{(t+1)} = \Psi_{p_i}(\boldsymbol{x}^{(t+1)} - \boldsymbol{d}_i^{(t)}, \frac{\lambda_i}{\mu})$;
4: $\quad \boldsymbol{d}_i^{(t+1)} = \boldsymbol{d}_i^{(t)} + \frac{1}{L'}(-\boldsymbol{x}^{(t+1)} + \boldsymbol{z}_i^{(t+1)})$;
5: $\quad \mathrm{res} = \|\boldsymbol{x}^{(t+1)} - \boldsymbol{x}^{(t)}\|_2 / \|\boldsymbol{x}^{(t)}\|_2$;
6: $\quad t = t + 1$;
7: **end while**

Output: $\hat{\boldsymbol{X}} = \boldsymbol{X}^{(t)}$.

3.2 Azimuth-range decouple-based fast sparse reconstruction

Considering the huge memory and computational cost caused by the large-scale measurement matrix $\boldsymbol{H}$, we adopt the CSA-based azimuth-range decouple operators as follows [1, 22]:

$$\mathcal{I}(\boldsymbol{Y}) = \boldsymbol{F}_a^{-1}\left(\boldsymbol{F}_a(\boldsymbol{Y}) \odot \boldsymbol{\Theta}_{\mathrm{sc}}\boldsymbol{F}_r \odot \boldsymbol{\Theta}_{\mathrm{rc}}\boldsymbol{F}_r^{-1} \odot \boldsymbol{\Theta}_{\mathrm{ac}}\right), \tag{16}$$

where $\mathcal{I}$ represents the imaging operator, $\boldsymbol{\Theta}_{\mathrm{sc}}$ is the phase matrix for differential range cell migration correction (RCMC) in CSA, $\boldsymbol{\Theta}_{\mathrm{rc}}$ is the phase matrix for range compression, secondary range compression (SRC) and bulk RCMC, and $\boldsymbol{\Theta}_{\mathrm{ac}}$ is the phase matrix for azimuth compression and phase correction. Multiplied by the Fourier matrix $\boldsymbol{F}_a$ or its inverse matrix $\boldsymbol{F}_a^{-1}$ on the left represents azimuth Fourier transform or inverse transform, multiplied by the Fourier matrix $\boldsymbol{F}_r$ or its inverse matrix $\boldsymbol{F}_r^{-1}$ on the right represents range Fourier transform or inverse transform.

And the inverse imaging operator $\mathcal{G}$ can be derived from the above imaging operator $\mathcal{I}$,

$$\mathcal{G}(\boldsymbol{X}) = \boldsymbol{F}_a^{-1}\left(\boldsymbol{F}_a(\boldsymbol{X}) \odot \boldsymbol{\Theta}_{\mathrm{ac}}^*\boldsymbol{F}_r \odot \boldsymbol{\Theta}_{\mathrm{rc}}^*\boldsymbol{F}_r^{-1} \odot \boldsymbol{\Theta}_{\mathrm{sc}}^*\right), \tag{17}$$

where $\boldsymbol{\Theta}_{\mathrm{ac}}^*$, $\boldsymbol{\Theta}_{\mathrm{rc}}^*$, and $\boldsymbol{\Theta}_{\mathrm{sc}}^*$ are the conjugate of $\boldsymbol{\Theta}_{\mathrm{ac}}$, $\boldsymbol{\Theta}_{\mathrm{rc}}$, and $\boldsymbol{\Theta}_{\mathrm{sc}}$.

The above azimuth-range decouple operators are able to substitute measurement matrix $\boldsymbol{H}$ and its Hermitian transpose in (13). In the actual implementation, as there are slight differences between the observation models of ℓ_1, ℓ_1-TV regularization and $\ell_{2,1}$ regularization, the combination with decouple operators will also be different.

For ℓ_1 and ℓ_1-TV regularization, the measurement matrix $\boldsymbol{H}$ consists of only one block; hence it is equivalent to the following CSA-based azimuth-range decouple operators [22]:

$$\boldsymbol{H}\boldsymbol{x} \cong \mathrm{vec}\left[\mathcal{G}(\boldsymbol{X})\right], \ \boldsymbol{H}^{\mathrm{H}}\boldsymbol{y} \cong \mathrm{vec}\left[\mathcal{I}(\boldsymbol{Y})\right]. \tag{18}$$

And then Eq. (13) can be written as the following two dimensional expression:

$$\boldsymbol{X}^{(t+1)} = \boldsymbol{X}^{(t)} + \frac{1}{L}\left[\frac{\mu}{2}\sum_i^N(\boldsymbol{Z}_i^{(t)} + \boldsymbol{D}_i^{(t)}) - \frac{\mu}{2}N\boldsymbol{X}^{(t)} + \mathcal{I}(\boldsymbol{Y} - \mathcal{G}(\boldsymbol{X}^{(t)}))\right]. \tag{19}$$

For $\ell_{2,1}$ regularization, the measurement matrix $\boldsymbol{H}$ consists of three blocks, corresponding to three couples of operators respectively, in which $\mathcal{G}_0, \mathcal{I}_0$ are operators of target area, and $\mathcal{G}_{\pm 1}, \mathcal{I}_{\pm 1}$ are operators of ± 1 ambiguity area [13]:

$$
\begin{aligned}
\boldsymbol{H}\boldsymbol{x} &= \begin{bmatrix}\boldsymbol{H}_{-1}, \boldsymbol{H}_0, \boldsymbol{H}_{+1}\end{bmatrix}\begin{bmatrix}\boldsymbol{x}_{-1}\\ \boldsymbol{x}_0\\ \boldsymbol{x}_{+1}\end{bmatrix} = \boldsymbol{H}_{-1}\boldsymbol{x}_{-1} + \boldsymbol{H}_0\boldsymbol{x}_0 + \boldsymbol{H}_{+1}\boldsymbol{x}_{+1}\\
&\cong \operatorname{vec}\left[\mathcal{G}_{-1}(\boldsymbol{X}_{-1}) + \mathcal{G}_0(\boldsymbol{X}_0) + \mathcal{G}_{+1}(\boldsymbol{X}_{+1})\right],\\
\boldsymbol{H}^{\mathrm{H}}\boldsymbol{y} &= \begin{bmatrix}(\boldsymbol{H}_{-1})^{\mathrm{H}}\\ (\boldsymbol{H}_0)^{\mathrm{H}}\\ (\boldsymbol{H}_{+1})^{\mathrm{H}}\end{bmatrix}\boldsymbol{y} \cong \begin{bmatrix}\operatorname{vec}\left[\mathcal{I}_{-1}(\boldsymbol{Y})\right]\\ \operatorname{vec}\left[\mathcal{I}_0(\boldsymbol{Y})\right]\\ \operatorname{vec}\left[\mathcal{I}_{+1}(\boldsymbol{Y})\right]\end{bmatrix}.
\end{aligned} \tag{20}
$$

Hereby Eq. (13) can be written as the following two dimensional expression:

$$
\begin{aligned}
\boldsymbol{X}^{(t+1)} = \begin{bmatrix}\boldsymbol{X}_{-1}^{(t+1)}\\ \boldsymbol{X}_{0}^{(t+1)}\\ \boldsymbol{X}_{+1}^{(t+1)}\end{bmatrix} &= \boldsymbol{X}^{(t)} + \frac{1}{L}\left[\frac{\mu}{2}\sum_{i}^{N}(\boldsymbol{Z}_i^{(t)} + \boldsymbol{D}_i^{(t)}) - \frac{\mu}{2}N\boldsymbol{X}^{(t)}\right.\\
&\left. + \begin{bmatrix}\mathcal{I}_{-1}(\boldsymbol{Y} - \mathcal{G}_{-1}(\boldsymbol{X}_{-1}^{(t)}) - \mathcal{G}_0(\boldsymbol{X}_0^{(t)}) - \mathcal{G}_{+1}(\boldsymbol{X}_{+1}^{(t)}))\\ \mathcal{I}_{0}(\boldsymbol{Y} - \mathcal{G}_{-1}(\boldsymbol{X}_{-1}^{(t)}) - \mathcal{G}_0(\boldsymbol{X}_0^{(t)}) - \mathcal{G}_{+1}(\boldsymbol{X}_{+1}^{(t)}))\\ \mathcal{I}_{+1}(\boldsymbol{Y} - \mathcal{G}_{-1}(\boldsymbol{X}_{-1}^{(t)}) - \mathcal{G}_0(\boldsymbol{X}_0^{(t)}) - \mathcal{G}_{+1}(\boldsymbol{X}_{+1}^{(t)}))\end{bmatrix}\right].
\end{aligned} \tag{21}
$$

Taking ℓ_1 regularization as the example, the azimuth-range decouple-based general ADMM for sparse reconstruction is summarized in Algorithm 2, which consists of two dimensional operations.

Algorithm 2 Azimuth-range decouple-based general ADMM for sparse reconstruction

Input: The echo data $\boldsymbol{Y}$, the initial solution $\boldsymbol{X}^{(0)} = \boldsymbol{0}$, $\boldsymbol{Z}_i^{(0)} = \boldsymbol{0}$, $\boldsymbol{D}_i^{(0)} = \boldsymbol{0}$, the azimuth-range decouple operators $\mathcal{G}$ and $\mathcal{I}$, the error parameter ϵ, and the minimum and maximum number of iteration $t \in [0, T_{\max}]$.

while res $\geqslant \epsilon$ and $t \leqslant T_{\max}$ **do**
- $\boldsymbol{X}^{(t+1)} = \boldsymbol{X}^{(t)} + \frac{1}{L}[\frac{\mu}{2}\sum_i^N(\boldsymbol{Z}_i^{(t)} + \boldsymbol{D}_i^{(t)}) - \frac{\mu}{2}N\boldsymbol{X}^{(t)} + \mathcal{I}(\boldsymbol{Y} - \mathcal{G}(\boldsymbol{X}^{(t)}))]$;
- $\boldsymbol{Z}_i^{(t+1)} = \Psi_{p_i}(\boldsymbol{X}^{(t+1)} - \boldsymbol{D}_i^{(t)}, \frac{\lambda_i}{\mu})$;
- $\boldsymbol{D}_i^{(t+1)} = \boldsymbol{D}_i^{(t)} + \frac{1}{L'}(-\boldsymbol{X}^{(t+1)} + \boldsymbol{Z}_i^{(t+1)})$;
- res $= \|\boldsymbol{X}^{(t+1)} - \boldsymbol{X}^{(t)}\|_{\mathrm{F}}/\|\boldsymbol{X}^{(t)}\|_{\mathrm{F}}$;
- $t = t + 1$;

end while

Output: $\hat{\boldsymbol{X}} = \boldsymbol{X}^{(t)}$.

3.3 Theoretical analysis of phase preservation

Benefiting from the approximate representation, the decouple operator-based algorithm and the measurement matrix-based algorithm have the equivalent phase preserving ability. Moreover, the operators establish an association between sparse reconstruction and CSA, which makes the analysis more simple and intuitive.

Hereby, we can illustrate the phase preservation of sparse reconstruction by analyzing Algorithm 2 step by step. For convenience, this paper takes zero initialization as an example for analysis. Thanks to the good convergence of the algorithm, taking other initial values can converge to the same optimal solution as taking zero initial value [21, 26]. Therefore, the following analysis is universal to arbitrary initial values:

• For $t = 0$, initialize $\boldsymbol{X}$, $\boldsymbol{Z}$, and $\boldsymbol{D}$ to 0; then

(1) $\boldsymbol{X}^{(t+1)}$: $\boldsymbol{X}^{(1)} = \frac{1}{L}\mathcal{I}(\boldsymbol{Y})$, which means the phase of $\boldsymbol{X}^{(1)}$ is consistent with that of CSA.

(2) $\boldsymbol{Z}_i^{(t+1)}$: the proximal operators for three kinds of penalties are listed in Table 1. Since Ψ only affects the amplitude without changing the phase [8, 9, 21], the phase of $\boldsymbol{Z}_i^{(1)}$ is consistent with that of $\boldsymbol{X}^{(1)}$.

• For $t \geqslant 1$, the above analysis results indicate that $\boldsymbol{X}^{(1)}$ and $\boldsymbol{Z}_i^{(1)}$ are phase preserving; then

(1) ℓ_1 and ℓ_1-TV regularization: since $\mathcal{I}$ and $\mathcal{G}$ are inverse operators, the expressions of $\boldsymbol{X}^{(t+1)}$ and $\boldsymbol{Z}_i^{(t+1)}$ only include the $\pm$ operation under the same phase condition and the amplitude-proximal operation based on $\frac{1}{L}\mathcal{I}(\boldsymbol{Y})$, $\boldsymbol{X}^{(1)}$, and $\boldsymbol{Z}_i^{(1)}$, without any operation that affects the phase preserving ability.

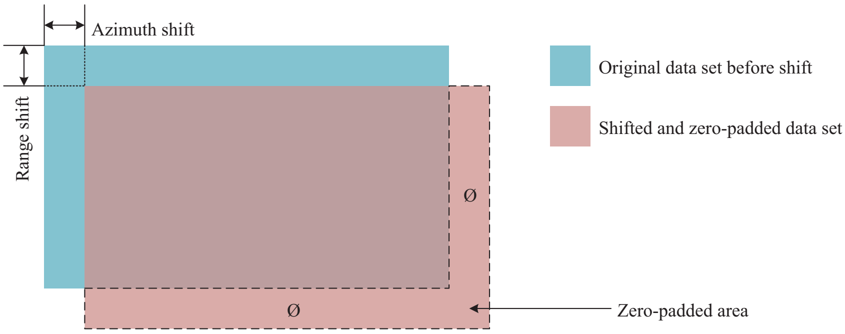

Figure 2 (Color online) Diagram of offset test.

Table 2 The evaluation criteria

Evaluation index	Requirement
Mean of interferogram phase (φ_0)	$\leqslant 0.1^\circ$
Standard deviation of interferogram phase (σ_φ)	$\leqslant 5.0^\circ$

Therefore, the sparse reconstruction results $\boldsymbol{X}^{(t+1)}$ always keep the same phase as $\mathcal{I}(\boldsymbol{Y})$, while suppressing the amplitude of additive noise and smoothing the amplitude of speckles. Furthermore, the phase preservation indexes of ℓ_1 and ℓ_1-TV regularization will be consistent with CSA.

(2) $\ell_{2,1}$ regularization: as there exist $\mathcal{I}_0(\mathcal{G}_{-1}(\boldsymbol{X}_{-1}^{(t)}))$ and $\mathcal{I}_0(\mathcal{G}_{+1}(\boldsymbol{X}_{-1}^{(t)}))$ in the expression of $\boldsymbol{X}^{(t+1)}$, the phase values and phase preservation indexes of $\ell_{2,1}$ regularization will be slightly different from CSA results $\mathcal{I}_0(\boldsymbol{Y})$. Nevertheless, thanks to the phase preservation of the ambiguity-area-operators $\mathcal{G}_{\pm 1}$, all processings in the expression of $\boldsymbol{X}_0^{(t+1)}$ are phase-preserving; therefore, the $\ell_{2,1}$ regularization still has the phase preserving ability.

In conclusion, according to the above theoretical analysis of our algorithm, we can preliminarily prove that the general ADMM framework-based sparse reconstruction has the same level of phase preserving ability as CSA.

4 Experiments and the interferometric offset test

4.1 Definition of the interferometric offset test

To validate the phase-preserving capability of sparse SAR imaging, the interferometric offset test must be conducted [18]. As shown in Figure 2 and Table 2, considering the accuracy requirements of phase in the interferometric and tomographic SAR [14], we need to evaluate the mean and standard deviation of the interferogram phase of the overlap-focused area.

4.2 Experimental results and analysis

In this subsection, the simulated and real GF-3 SAR data are used to validate the phase preservation of sparse reconstruction.

In the simulation, we have arranged three sets of 2048×2048 scenarios, and generated raw echo data respectively under the condition of signal to noise ratios (SNRs) $= -30, -20, -30$ dB. We used representative spaceborne SAR parameters in the experimental setup: the altitude of the simulated SAR platform was 800 km, and the slant range of the scene center was 850 km. The main SAR system parameters are listed in Table 3. Simulation data were obtained by generating echoes from each point in the observation scene and stacking them linearly.

In Scene 1, we placed 9 point targets in the scene center and employed CSA and ℓ_1 regularization to reconstruct the scene. As shown in column 1 in Figure 3, ℓ_1 regularization can significantly suppress additive noise. In Scene 2, we placed a distributed target in the scene center. According to [27], we set an equivalent phase center in each pixel cell of the distributed target; their amplitudes were independent and identically distributed Rayleigh random variables with mean $\mu = \sqrt{\pi\sigma_0/2}$ and standard deviation $\sigma = \sqrt{(1-\pi/4)\sigma_0}$ (σ_0 is the backscattering coefficient) and their phases were uniformly distributed over

Table 3 The main SAR system parameters in the simulation

Parameter	Value	Unit
Carrier frequency	5.3	GHz
Pulse duration	40	μs
Range frequency modulation rate	0.5	MHz/μs
Range sampling rate	24	MHz
Antenna length	10	m
Effective radar velocity	7100	m/s
Pulse repetition frequency (PRF)	1700	Hz

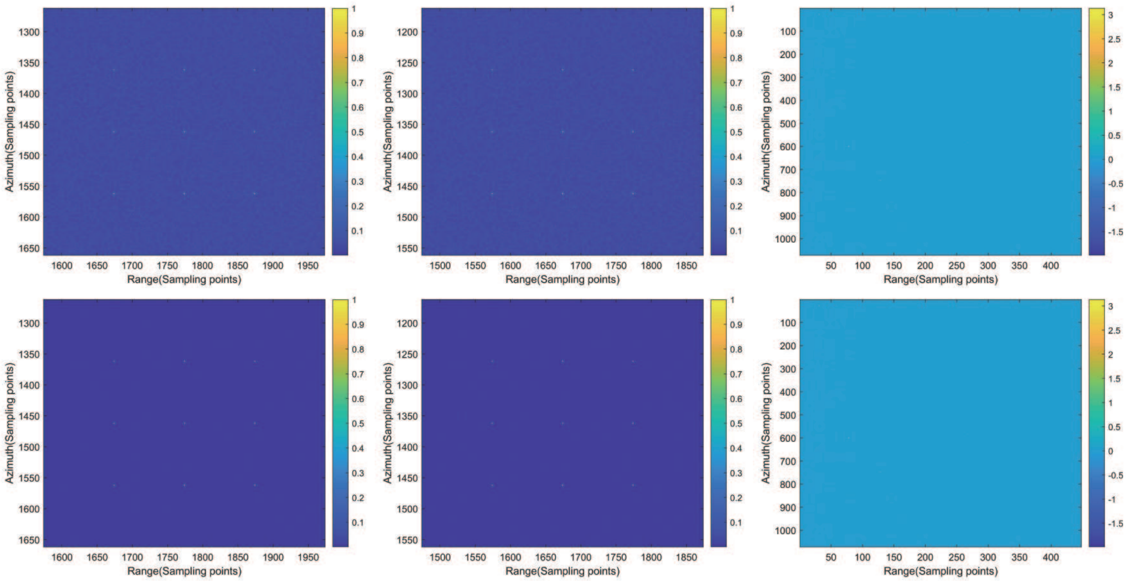

Figure 3 (Color online) Imaging results (°) of the simulated Scene 1 SAR data. Column 1: before shift; column 2: after shift; column 3: interferometric phase. Row 1: CSA; row 2: ℓ_1.

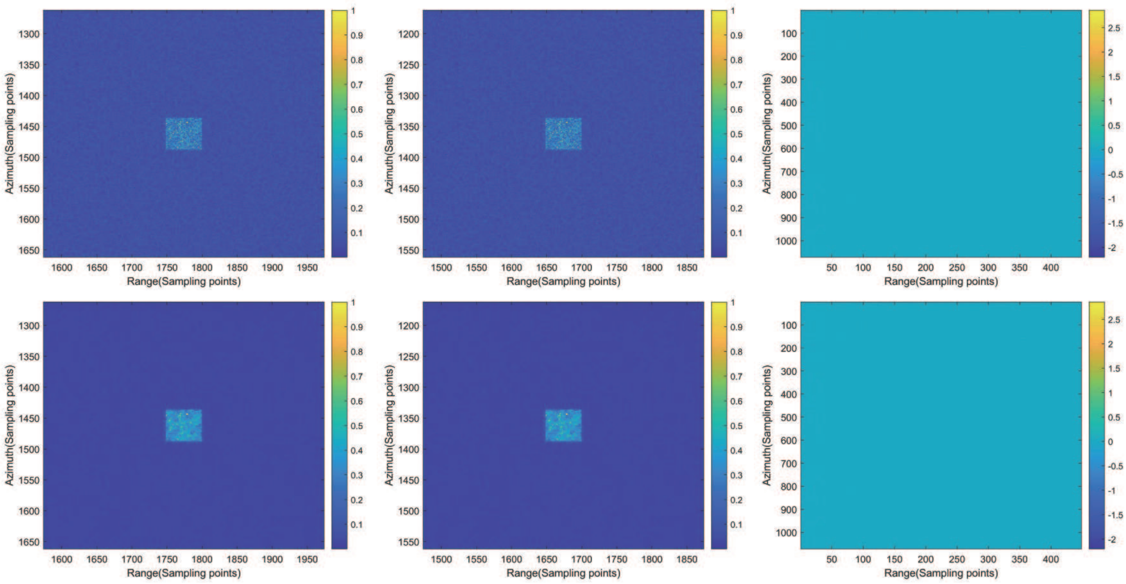

Figure 4 (Color online) Imaging results (°) of the simulated Scene 2 SAR data. Column 1: before shift; column 2: after shift; column 3: interferometric phase. Row 1: CSA; row 2: ℓ_1-TV.

$[-\pi, +\pi)$. Next, we employed CSA and ℓ_1 regularization to reconstruct the scene [27]. As shown in column 1 in Figure 4, ℓ_1-TV regularization could suppress speckles and additive noise.

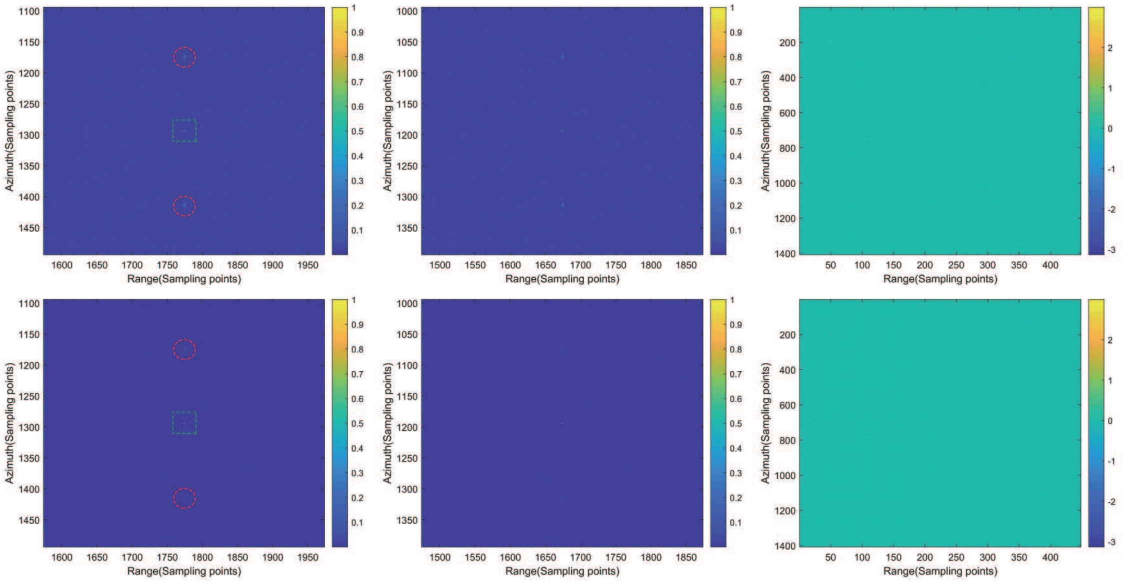

Figure 5 (Color online) Imaging results (°) of the simulated SAR data. Column 1: before shift; column 2: after shift; column 3: interferometric phase. Row 1: CSA; row 2: $\ell_{2,1}$.

Table 4 Offset test results of the simulated SAR data

	Scene 1		Scene 2		Scene 3	
	CSA	ℓ_1	CSA	ℓ_1-TV	CSA	$\ell_{2,1}$
φ_0 (°)	2.1236×10^{-4}	2.1236×10^{-4}	2.1756×10^{-4}	2.1756×10^{-4}	7.6168×10^{-4}	6.7699×10^{-4}
σ_φ (°)	1.2548	1.2548	1.1848	1.1848	1.1574	1.1601

In Scene 3, we placed a point target (labeled by the green dotted box) and performed 50% uniform down-sampling in the azimuth direction. As shown in column 1 in Figure 5, there are obvious ambiguities in the CSA results labeled by red dotted circles, while $\ell_{2,1}$ regularization can effectively suppress ambiguities.

Then, we set the azimuth and range shift to 100 lines/points, cut, and zero-padded the original data. Next we repeat the above imaging processing on these shifted data, and the results are shown in column 2 in Figures 3–5.

Finally, we conducted the interferometric offset test on the imaging results and obtained the interferogram phase as shown in column 3 in Figures 3–5. Further, we calculated the mean and standard deviation of the interferogram phase, as shown in Table 4. Evidently, ℓ_1, ℓ_1-TV, and $\ell_{2,1}$ regularization meet the requirements of phase preservation. The indices of ℓ_1 and ℓ_1-TV are similar to those of CSA, whereas that of $\ell_{2,1}$ is slightly different, which is consistent with the analysis presented in Subsection 3.3.

GF-3 is the first C-band remote sensing satellite with quad-polarization and multiangle capability in the civilian field of China. It operates with 12 imaging modes and a spatial resolution of up to 1 m, and its remote sensing data are extensively utilized and recognized in China. In this experiment, the StripMAP mode data with HH polarization were used.

In the processing of real GF-3 SAR data, we selected an area containing points as well as distributed targets as the experimental scene. For full sampling, we employed CSA, ℓ_1, and ℓ_1-TV regularization to reconstruct the scene. Similarly, for down-sampling, we employed CSA and $\ell_{2,1}$ regularization to reconstruct the scene. Experimental results shown in column 1 in Figures 6 and 7 reveal that sparse reconstruction methods can suppress noise, speckle, and ambiguity (labeled by red, blue, and green dotted boxes).

Next, we set the azimuth and range shift to 100 lines/points, cut, and zero-padded the original data. Subsequently, we repeated the imaging process on the shifted data, as shown in column 2 in Figures 6 and 7.

Finally, the interferometric offset test was conducted on the imaging results of real SAR data. The interferogram phase in column 3 in Figures 6 and 7 and the calculated φ_0, σ_φ in Table 5 validated the phase preservation of ℓ_1, ℓ_1-TV, and $\ell_{2,1}$ regularizations in real SAR data processing.

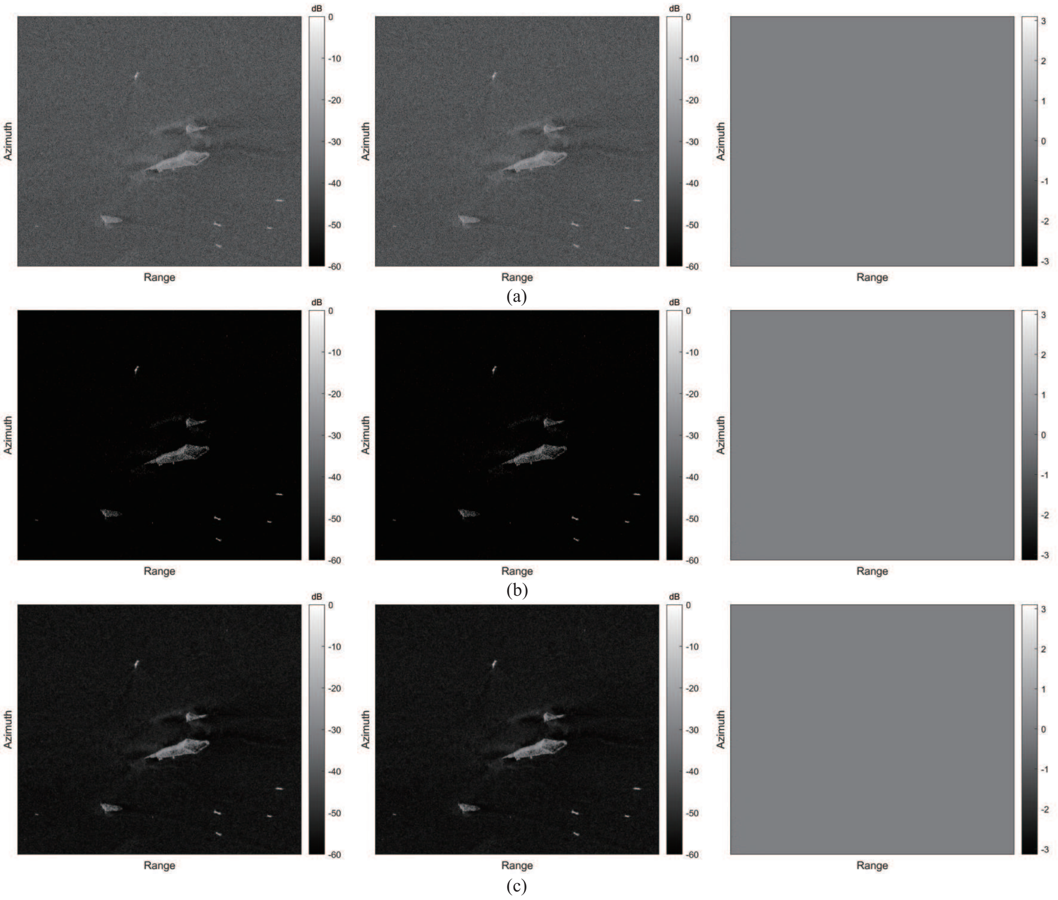

Figure 6 Imaging results (°) of GF-3 SAR data under the full sampling condition. Column 1: before shift; column 2: after shift; column 3: interferometric phase. (a) CSA; (b) ℓ_1; (c) ℓ_1-TV.

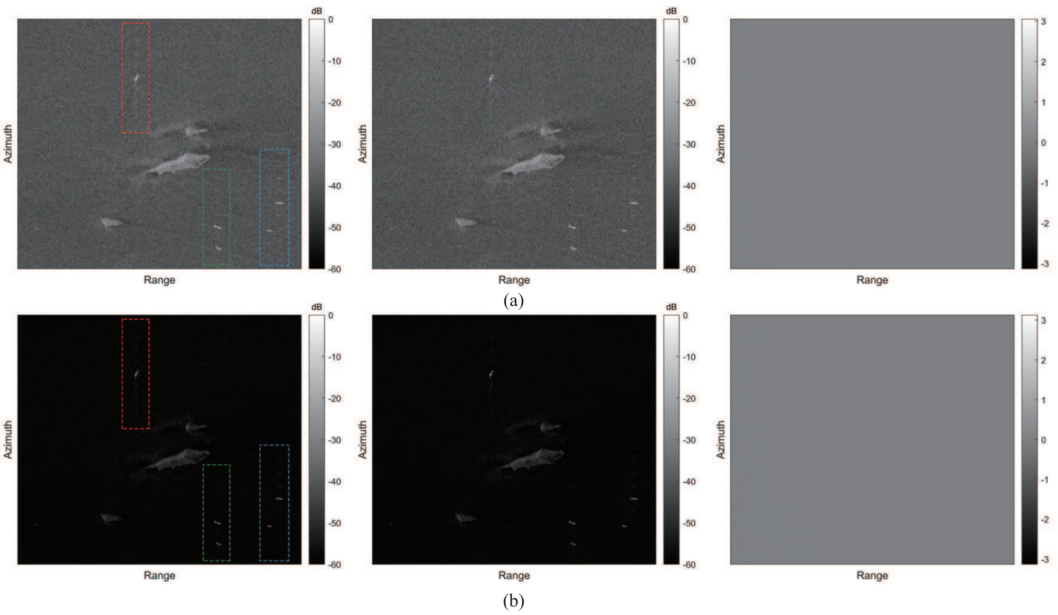

Figure 7 Imaging results (°) of GF-3 SAR data under the down-sampling condition. Column 1: before shift; column 2: after shift; column 3: interferometric phase. (a) CSA; (b) $\ell_{2,1}$.

Table 5 Offset test results of the real GF-3 SAR data

	CSA full sampling	ℓ_1	ℓ_1-TV	CSA down-sampling	$\ell_{2,1}$
φ_0 (°)	2.9550×10^{-4}	2.9550×10^{-4}	2.9550×10^{-4}	8.7895×10^{-4}	5.2193×10^{-4}
σ_φ (°)	1.8161	1.8161	1.8161	1.8796	1.8801

5 Conclusion

In this study, we evaluated the phase preservation of sparse SAR imaging for applying two-dimensional sparse reconstruction results in polarimetric, interferometric, and tomographic SAR. We considered ℓ_1, ℓ_1-TV, and $\ell_{2,1}$ regularizations as examples and theoretically analyzed the phase preservation of sparse reconstruction algorithm, which was represented by the general ADMM framework based on azimuth-range decouple, through a comparison with the reconstruction results of CSA. Finally, we processed the simulated and real GF-3 SAR data and conducted the interferometric offset test on sparse SAR imaging results. The results of experiments and analysis verified the phase-preserving capability of sparse reconstruction. Based on the results of this study, we will utilize the sparse reconstruction results for more in-depth research in the future.

Acknowledgements This work was supported by National Natural Science Foundation of China (Grant No. 61991421).

References

1 Zhang B C, Hong W, Wu Y R. Sparse microwave imaging: principles and applications. Sci China Inf Sci, 2012, 55: 1722–1754
2 Ender J H G. On compressive sensing applied to radar. Signal Processing, 2010, 90: 1402–1414
3 Zhang L, Xing M, Qiu C W, et al. Resolution enhancement for inversed synthetic aperture radar imaging under low SNR via improved compressive sensing. IEEE Trans Geosci Remote Sens, 2010, 48: 3824–3838
4 Yang J, Thompson J, Huang X, et al. Random-frequency SAR imaging based on compressed sensing. IEEE Trans Geosci Remote Sens, 2012, 51: 983–994
5 Bi H, Zhang B, Zhu X X, et al. Extended chirp scaling-baseband azimuth scaling-based azimuth-range decouple L_1 regularization for TOPS SAR imaging via CAMP. IEEE Trans Geosci Remote Sens, 2017, 55: 3748–3763
6 Bi H, Zhang B, Zhu X X, et al. Azimuth-range decouple-based L_1 regularization method for wide ScanSAR imaging via extended chirp scaling. J Appl Remote Sens, 2017, 11: 015007
7 Elad M. Sparse and Redundant Representations: From Theory to Applications in Signal and Image Processing. New York: Springer, 2010
8 Chambolle A. An algorithm for total variation minimization and applications. J Math Imag Vision, 2004, 20: 89–97
9 Zhang B C, Jiang C L, Zhang Z. Azimuth ambiguity suppression for SAR imaging based on group sparse reconstruction. In: Proceedings of the 2nd International Workshop on Compressed Sensing Applied to Radar, 2013. 17–19
10 Candés E J. The restricted isometry property and its implications for compressed sensing. Comptes Rendus Mathematique, 2008, 346: 589–592
11 Bi H, Li Y, Zhu D Y, et al. An improved iterative thresholding algorithm for L1-norm regularization based sparse SAR imaging. Sci China Inf Sci, 2020, 63: 219301
12 Xu Z, Zhang B, Zhang Z, et al. Nonconvex-nonlocal total variation regularization-based joint feature-enhanced sparse SAR imaging. IEEE Geosci Remote Sens Lett, 2022, 19: 1–5
13 Quan X, Zhang B, Zhu X X, et al. Unambiguous SAR imaging for nonuniform DPC sampling: ℓ_q regularization method using filter bank. IEEE Geosci Remote Sens Lett, 2016, 13: 1596–1600
14 Rambour C, Budillon A, Johnsy A C, et al. From interferometric to tomographic SAR: a review of synthetic aperture radar tomography-processing techniques for scatterer unmixing in urban areas. IEEE Geosci Remote Sens Mag, 2020, 8: 6–29
15 Çetin M, Stojanović I, Önhon N Ö, et al. Sparsity-driven synthetic aperture radar imaging: reconstruction, autofocusing, moving targets, and compressed sensing. IEEE Signal Process Mag, 2014, 31: 27–40
16 Xu Z, Zhou G, Zhang B, et al. Sparse regularization method combining SVA for feature enhancement of SAR images. Electron Lett, 2022, 58: 591–593
17 Wei Z H, Zhang B C, Wu Y R. A SAR imaging method based on generalized minimax-concave penalty. Sci China Inf Sci, 2019, 62: 029305
18 Tell B R, Laur H. Phase preservation in SAR processing: the interferometric offset test. In: Proceedings of IEEE International Geoscience and Remote Sensing Symposium, 1996. 1: 477–480
19 Belotti M, D'Aria D, Guccione P, et al. Requirements and tests for phase preservation in a SAR processor. IEEE Trans Geosci Remote Sens, 2013, 52: 2788–2798
20 Boyd S, Parikh N, Chu E, et al. Distributed optimization and statistical learning via the alternating direction method of multipliers. FNT Machine Learn, 2010, 3: 1–122

21 Güven H E, Güngör A, Cetin M. An augmented lagrangian method for complex-valued compressed SAR imaging. IEEE Trans Comput Imag, 2016, 2: 235–250

22 Fang J, Xu Z, Zhang B, et al. Fast compressed sensing SAR imaging based on approximated observation. IEEE J Sel Top Appl Earth Observations Remote Sens, 2013, 7: 352–363

23 Raney R K, Runge H, Bamler R, et al. Precision SAR processing using chirp scaling. IEEE Trans Geosci Remote Sens, 1994, 32: 786–799

24 Afonso M V, Bioucas-Dias J M, Figueiredo M A T. Fast image recovery using variable splitting and constrained optimization. IEEE Trans Image Process, 2010, 19: 2345–2356

25 Xu Z, Zhang B, Zhou G, et al. Sparse SAR imaging and quantitative evaluation based on nonconvex and TV regularization. Remote Sens, 2021, 13: 1643

26 Calafiore G C, Ghaoui L E. Optimization Models. Cambridge: Cambridge University Press, 2014

27 Oliver C, Quegan S. Understanding Synthetic Aperture Radar Images. Valencia: SciTech Publishing, 2004